Chapter 2
Exotic Behavior in Quantum Dot Mode-Locked Lasers: Dark Pulses and Bistability

Kevin Silverman, Mingming Feng, Richard Mirin and Steven Cundiff

Abstract Passively mode-locked semiconductor lasers with self-assembled quantum dot active regions can be operated in exotic output modes, stabilized by the complex gain and absorption dynamics inherent in these structures. One such device emits dark pulses—sharp dips on an otherwise stable continuous wave background—in an extended cavity design. We show that a dark pulse train is a solution to the master equation for mode-locked lasers and perform numerical modeling to test the stability of such a solution. A separate, monolithic design displays wavelength bistability and can be electrically switched between these two modes within just a few cavity round trips. This device can be made to switch between two stable wavelengths separated by just 7 nm up to over 40 nm with a contrast ratio of over 40 dB.

K. Silverman (✉) · M. Feng · R. Mirin
Optoelectronics Division, National Institute of Standards and Technology, Boulder, CO 80305, USA
e-mail: silverma@boulder.nist.gov; kevin.silverman@nist.gov

M. Feng
e-mail: mingming@boulder.nist.gov

R. Mirin
e-mail: mirin@boulder.nist.gov

S. Cundiff
Quantum Physics Division, JILA, National Institute of Standards and Technology and University of Colorado, Boulder, CO 80305, USA
e-mail: cundiffs@nist.gov

Z. M. Wang (ed.), *Quantum Dot Devices*, Lecture Notes in Nanoscale Science and Technology 13, DOI: 10.1007/978-1-4614-3570-9_2,

Introduction

Background

Mode-locked lasers have become an essential tool in both industrial applications and scientific investigations. They are capable of generating ultrashort pulses (down to below 10 fs) enabling ultra-high peak powers and unbeatable time resolution of optically generated excitations in a wide variety of materials. There are many applications of ultrashort/broadband optical pulses that are hindered by the cost, complexity, and inefficiency of the mode-locked lasers used to produce such pulses. This reasoning led to significant effort in mode-locked diode lasers 10–15 years ago. However, these efforts ran up against a fundamental barrier that limited the brevity of the pulses, falling well short of the performance required for the most promising applications. Initially, diode lasers based on self-assembled quantum dots (QDs) were proposed to break this barrier. This optimism was fuelled by two unique properties of QDs. First, the large gain bandwidth (up to over 100 nm) of these materials, attributable to the inherent size and composition distribution of the individual QDs could easily support ultrashort pulses. Second, it was theorized that QDs would have a very small linewidth enhancement factor (LEF) because of the symmetric gain coefficient attributable to 3D confinement [1, 2]. The LEF determines the amount of nonlinear chirp imparted on the mode-locked pulse during amplification and seriously limits the duration and quality of the pulses generated [1]. After long attempts by many groups, using monolithic [3] and extended cavity schemes, QD mode-locked diode lasers have failed to reach the ultrashort pulse regime, although small improvements over quantum well material have been realized. Subsequent measurements have revealed that the gain dynamics in the QD active region under normal operating conditions are not as simple as initially thought. For instance, it has been shown that the LEF is not only significant, but that it has a strong dependence on carrier injection levels [4]. As is often the case, it turns out that these unwanted, unanticipated, properties lead to unexpected, exciting performance as well. Two such novel operating regimes discovered in QD-based mode-locked lasers are the subjects of this chapter.

QD Gain Chip

The design of the QD gain chip for both monolithic and extended cavity structures is that of a standard double heterostructure laser. The active region consists of a 10-fold stack of InGaAs QD layers embedded in a GaAs waveguide, which is sandwiched between AlGaAs cladding layers. A cross section detailing the layer growth and etch profile is displayed in Fig. 2.1. The upper and lower AlGaAs cladding is doped to facilitate current injection.

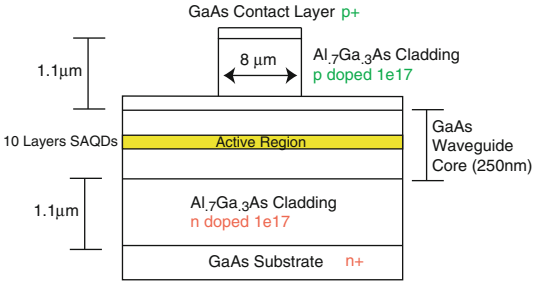

Fig. 2.1 Layer structure for the epitaxial material used in this work

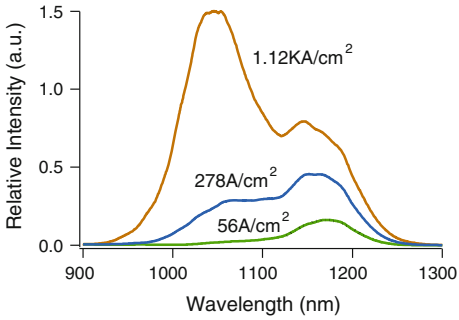

Fig. 2.2 Electroluminescence at various injection levels collected from the AR-coated QD gain chip

Standard photolithography and wet etching were used to etch a ridge into the top cladding layer. Electroluminescence from a typical device is displayed in Fig. 2.2. Clearly evident is the exceptionally large gain bandwidth mentioned in the Introduction. Also present is a strong rise in the excited state (ES) emission at higher injection levels due to state-filling effects. With inclusion of ES emission, the luminescence bandwidth of this device is greater than 150 nm. The ground-state transition alone has sufficient broadening to generate sub-100 fs pulses if used to its full potential.

Gain and Absorption Dynamics

Key to understanding the novel effects in a QD mode-locked laser is a detailed knowledge of the gain and absorption dynamics. It is the details of these processes that are responsible for stabilizing dark pulses and providing an appropriate operating region for bistable operation. It is therefore necessary to measure these properties of the laser material under operating conditions as close to the actual operating conditions as possible. The standard method for resolving these dynamics is ultrafast differential transmission spectroscopy, and many excellent reviews of the technique are available [5]. The experiment involves inducing a non-equilibrium carrier population in the gain medium with a resonant ultrafast laser pulse and then probing the decay of this excitation with a second time-delayed version of the pulse. All time-

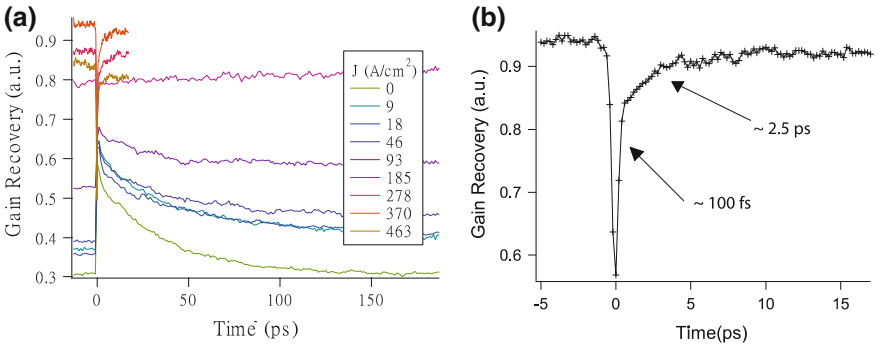

Fig. 2.3 **a** Recovery dynamics of the QD waveguide under various injection conditions. Current increases from *bottom* of figure to *top*. **b** Close-up view of the gain recovery at 278 A/cm^2

resolved data shown in this section was collected with differential transmission spectroscopy. Samples were antireflection coated or angle-cleaved in order to inhibit lasing at injection levels typical for laser operation.

Unfortunately, the desire to perform measurements on actual laser chips necessitates a substantial increase in the complexity of the DT measurement as compared to standard approaches. The difficulty arises when attempting to separate the pump from probe pulses for background-free detection of the probe transmission. The pump and probe propagate co-polarized through the QD waveguide in the same spatial mode. Therefore, the standard techniques of selecting the probe beam by its polarization or k-vector is not applicable. We choose to circumvent this problem by using a heterodyne pump-probe scheme as detailed by Hall et al. [6]. We give the probe beam a small frequency shift with an acousto-optic modulator and then beat the output of the waveguide with a local oscillator (LO) beam that does not interact with the sample. The probe beam can then be detected, without contamination from the pump beam, as a 60 MHz beat note between probe and LO.

Gain Recovery Dynamics

To investigate the recovery dynamics of the QD gain medium a positive bias must be applied to the p-i-n diode structure. Figure 2.3 shows differential transmission traces with the QD chip biased to different current densities. For reference, the transparency current density of this device is about 180 A/cm^2. Below this injection level the QDs are absorbing. When the current is higher than the transparency density, the QDs provide gain.

In Fig. 2.3a, the gain recovery dynamics at various injection levels is displayed. At time t = 0 the first pulse arrives and modifies the QD states. This depletes some of the gain (or saturates absorption), resulting in decreased (increased) transmission through the waveguide. There is a stark contrast between the dynamics

observed above and below transparency. Below transparency the absorption recovers by a combination of radiative recombination of photo-generated carriers and redistribution of those carriers over all dots in the ensemble. These are relatively slow processes proceeding on the 50 ps–1 ns timescale. The gain, on the other hand, recovers via the refilling of the active states from either ESs of the same dot or extended states that couple to all dots simultaneously. Recovery is clearly seen to proceed on two different, extremely fast, timescales. This is evident from Fig. 2.3a, in which the early time evolution of the QD population is shown in detail for a current bias of 278 A/cm^2. These two components of the decay can be extracted from the traces by fitting to a biexponential function. In general, the ultrafast response remains fairly constant over a broad range of currents above transparency with a value around 100 fs, possibly resolution limited. The second time constant indicated in Fig. 2.3b is in the single picosecond range and has a weak, but observable, dependence on injection current. In addition to the ultrafast processes, a longer recovery time, usually greater than 100 ps, is also observed.

QD gain recovery is usually described as proceeding in three steps: (1) intra-dot relaxation (sub-picoseconds), (2) carrier capture from the wetting layer to the dots (picoseconds), and (3) overall recovery of the carrier density of the electron injection on a timescale of hundreds of picoseconds. Dynamics on multiple timescales in QD gain materials are a unique property compared to other semiconductor gain materials.

Absorption Recovery Dynamics

When the QD ridge waveguide is reverse biased, it becomes a saturable absorber. The recovery dynamics of a QD saturable absorber differs dramatically from the case of a QD amplifier as the dots are initially empty, and photo-generated carriers fill the ground-state hole and electron levels. There is very little interaction with the wetting layer and ES carriers that dominates the response under carrier injection. We systematically investigated the recovery behavior of a QD saturable absorber with a pump-probe technique.

Pump-probe traces in transmission at different reverse bias voltages are shown in Fig. 2.4a. The traces are fitted with a biexponential function, where T_{a1} and T_{a2} are the two fast-recovery time constants, and A_{a1} and A_{a2} are the amplitudes. The results of the fitting time constants and amplitudes are shown in Fig. 2.4b. The plots show a picosecond-range, bias-independent recovery (T_{a1}) followed by a slower recovery (T_{a2}) decreasing from 38 to 2 ps as the reverse bias is increased from 0 to -9 V. When the reverse bias is higher than -4 V, the fast recovery time dominates the process. The shortest recovery time is 680 fs when the reverse bias is -9 V.

This behavior is consistent with a model [7] in which a QD's absorption recovery is considered to be the result of a combination of (1) fast thermal excitation of the injected ground-state carriers to higher states and (2) tunneling of the

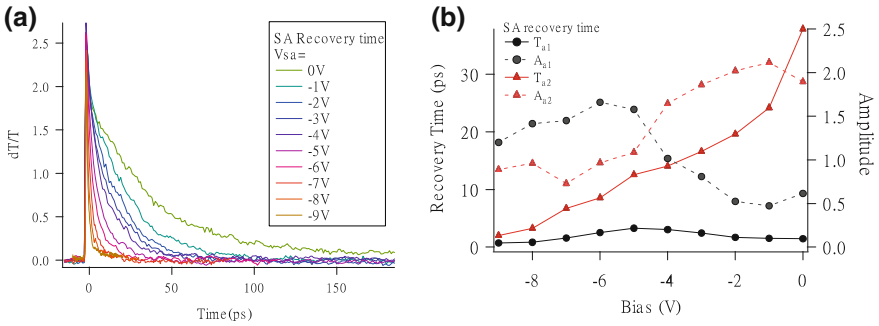

Fig. 2.4 **a** Absorption recovery dynamics for various reverse biases. Recovery duration decreases monotonically with increasing reverse bias. **b** Results of bi-exponential fit to the data displayed in **a**

excited carriers out of the dot. The timescale of the former process is bias independent, while the latter process becomes faster with increasing reverse bias. When bias is lower than −5 V, the tunneling of the carriers dominates the recovery of absorption. When the bias is higher than −5 V, thermal excitation is the primary process.

Our measured recovery times are comparable to those reported for a QD saturable absorber [8, 9]. In shallower dots, a shorter recovery time has been seen [10], which was interpreted as thermal escape.

Quantum dots under strong electric fields are powerful tools when used as saturable absorbers in mode-locked lasers. Under appropriate bias they display fast, sub-picosecond recovery dynamics capable of supporting 100 fs pulses. The fast recovery dynamics are promising for the optimization of saturable absorbers used for passive mode-locking of semiconductor lasers with ultrashort pulses and high repetition-rate pulses.

Dark Pulse Laser

Here, we discuss the first novel effect attributable to the unique gain dynamics in self-assembled QDs: the dark pulsed laser. Furthermore, we show that a dark pulse is a straightforward solution to the linearized version of the equation that describes the operation of a passively mode-locked laser [11]. To determine whether the solution is stable, and over what range of parameters, we perform simulations for the full (not linearized) equation. We show that the parameters of our laser fall in the range predicted to have stable dark pulses.

Dark pulses received considerable interest some years ago for their potential in the field of optical communications. When properly prepared as dark solitons, they propagate without distortion in material of normal dispersion [12], potentially opening up new transmission frequency choices for certain protocols [12].

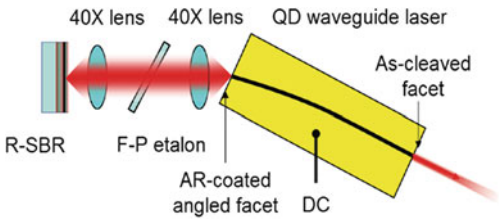

Fig. 2.5 Schematic of the extended-cavity semiconductor laser used for *dark* pulse generation. *R-SBR* resonant saturable absorber, *F–P* Fabry–Perot

Early attempts at generating dark pulses were made with bright pulse sources and external pulse shaping [13, 14]. Only recently, by our group and one other [15], have true mode-locked dark pulses been emitted directly from a laser. These recent successes have also led to some theoretical work into determining the conditions necessary for dark pulse generation [16].

We use an external cavity semiconductor diode laser to demonstrate the generation of dark pulses (Fig. 2.5). The gain section is a 5 mm long single-mode semiconductor ridge waveguide with InAs self-assembled QDs buried in the core. Light amplified by the QD active region is collimated, filtered by a Fabry–Perot etalon and focused on a saturable absorber to initiate mode-locking. The saturable absorbing medium, a few intentionally damaged semiconductor quantum wells, is grown in an integrated resonant structure to increase the electric field intensity and lower the saturation fluence. The saturable absorber structure also acts as an end mirror for the laser cavity. Spectral filtering to tune and restrict the lasing bandwidth was provided by a Fabry–Perot etalon with a transmission bandwidth of 10 nm. The flat facet of the semiconductor diode is used as the output coupler and has a reflectivity of approximately 30%. When the laser cavity is well aligned, lasing action occurs with 60 mA of current injected into the gain medium.

We monitored the output of the laser using a fast photodetector and recorded the output on a high-speed oscilloscope (shown in Fig. 2.6). A dark pulse train is clearly observed. The width of the pulses is measured to be 92 ps (a fit is shown in red in Fig. 2.6) and the modulation depth is approximately 70% [the ratio of the depth of the dark pulse to continuous wave (CW) level]. The clear comb confirmed the stability of the pulse train with narrow lines in the radio frequency spectrum of the photodiode output (shown in Fig. 2.6). We carefully calibrated the measurement system with a source of ultrafast bright pulses and determined the time resolution of our system to be about 60 ps, mostly limited by the sampling oscilloscope. This calibration also confirms that the signal is due to dark pulses and not artifacts of the detection system. A simple deconvolution of the instrument response function yields a true pulse width of 70 ps. Some ringing is evident in the signal for both dark and bright pulses, as is typically the case. Based on the calibration, we conclude that the pulses are dark pulses, although they are not "black" pulses, i.e., going to zero power, but rather "gray" pulses. The contrast ratio and modulation depth depend on the lasing wavelength (see supplementary material). Optical feedback into diode lasers can also result in trains of intensity dips that are attributed to coherence collapse [17, 18]. While there may be a

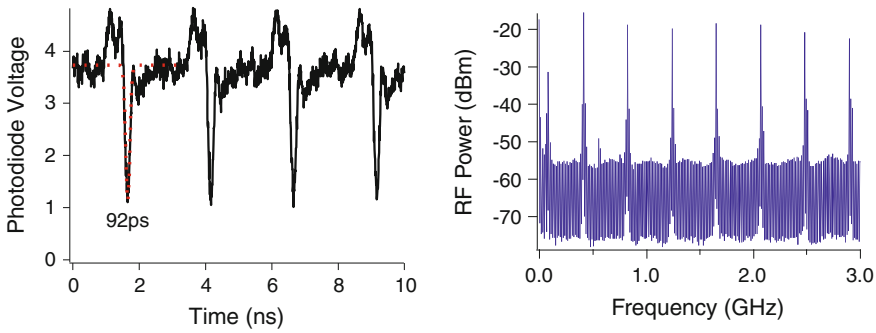

Fig. 2.6 Pulse train emitted from the *dark* pulse laser shown in the time and frequency domain

connection to our observations, the situation is quite different. Coherence collapse occurs when weak feedback is introduced to a chip-scale diode laser already above threshold. Our chip will not lase without the strong feedback from the extended cavity under any of the injection levels explored here, and pulsed operation does not occur without a saturable absorber in the cavity.

The question now becomes, what makes it possible for this dark pulse to exist? We can begin to understand the process by analogy with bright laser pulses. When a bright pulse interacts with a saturable absorbing medium, the pulse is shortened due to the increased transmission of the high intensity portion on the pulse with respect to the lower energy "wings". Now, let us assume that the saturable medium is already highly saturated by continuous radiation. If a small dark pulse interacts with this absorber it will be shortened as well, as the lower intensity portion on the pulse receives increased attenuation as the absorber is pulled out of saturation. We have shown this schematically in Fig. 2.7. This is the basic idea behind dark pulse generation. We will show later that our absorber is already in a highly saturated regime under CW excitation. In the following we will take a more formal approach to dark pulse generation, which confirms our basic understanding of the process and reveals the conditions necessary for observing this effect.

The theoretical understanding of mode-locked lasers typically starts from the "master equation" model developed by Haus [11]. In steady state, the pulse must reproduce itself every round trip. Considering only fast saturable gain, fast saturable absorption and spectral filtering due to the finite gain bandwidth yields the steady-state condition where u is the pulse amplitude, q (g) is the small-signal absorption (gain) coefficient normalized to the non-saturable loss in the cavity, E_a (E_g) is the saturation intensity for the absorber (gain), and ${\omega_g}^2$ is the gain bandwidth. This equation cannot be solved analytically, so we start by linearizing the gain and absorption saturation terms, giving

$$\left[1+\frac{q}{1+|u|^2\Big/E_a}-\frac{g}{1+|u|^2\Big/E_g}-\frac{g}{\omega_g^2}\frac{d^2}{dt^2}\right]u=0 \tag{2.1}$$

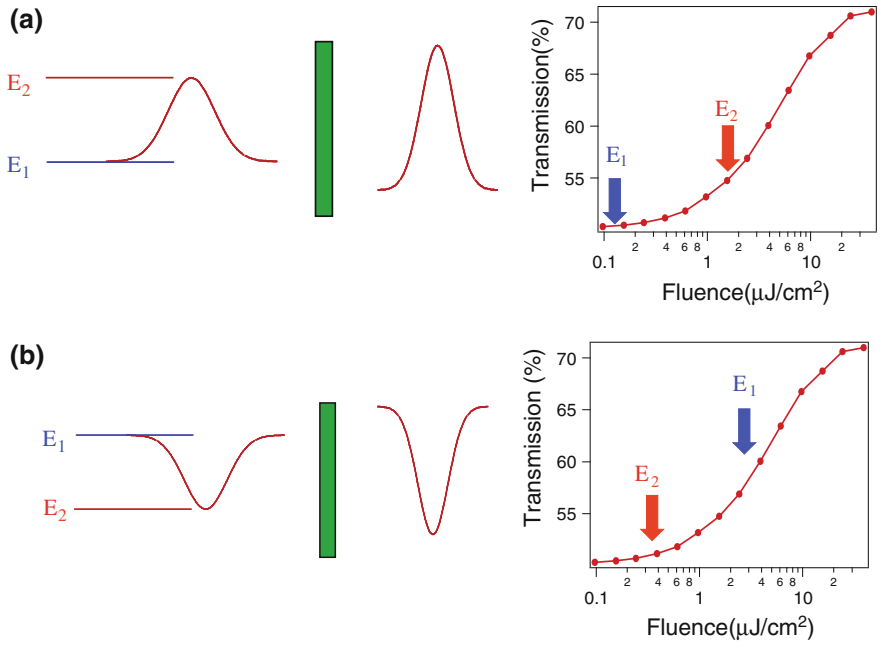

Fig. 2.7 Cartoons describing pulse shaping via interaction with a saturable absorber. **a** Conventional *bright* pulse shaping mechanism. **b** *Dark* pulse being accentuated by interacting with an absorber in a high degree of saturation

where u is the pulse amplitude, q (g) is the small-signal absorber (gain) coefficient normalized to the non-saturable loss in the cavity, E_a (E_g) is the saturation intensity for the absorber (gain), and ${\omega_g}^2$ is the gain bandwidth. This equation cannot be solved analytically, so we start by linearizing the gain and absorption saturation terms, giving

$$\left[1 + q\left(1 - \frac{|u|^2}{E_a}\right) - g\left(1 - \frac{|u|^2}{E_a}\right) - \frac{g}{\omega_g^2}\frac{d^2}{dt^2}\right]u = 0 \tag{2.2}$$

A solution to this equation has the form of $u = u_0 \tanh(\tau/\tau_p)$. This solution corresponds to a CW wave of amplitude u_0 with a dip at $t = 0$ that has a width τ_p. The CW wave before the dip has a π phase shift compared to that after the dip. While this analysis shows that a dark pulse is a solution, it does not show that it is stable against perturbations, which is also a requirement for it to exist in a physical system such as a laser. Stability arises from the interplay of saturation and the spectral filtering. The linearized equation does not adequately capture the interplay, indeed bright pulses are not stable solutions. To study stability, we resort to numerical simulations of Eq. 2.1.

In a numerical simulation, additional terms can be added to more accurately model the real laser. This includes the biexponential gain recovery of QDs. We attribute these times to intra-dot relaxation and to refilling of the dots from the wetting layer,

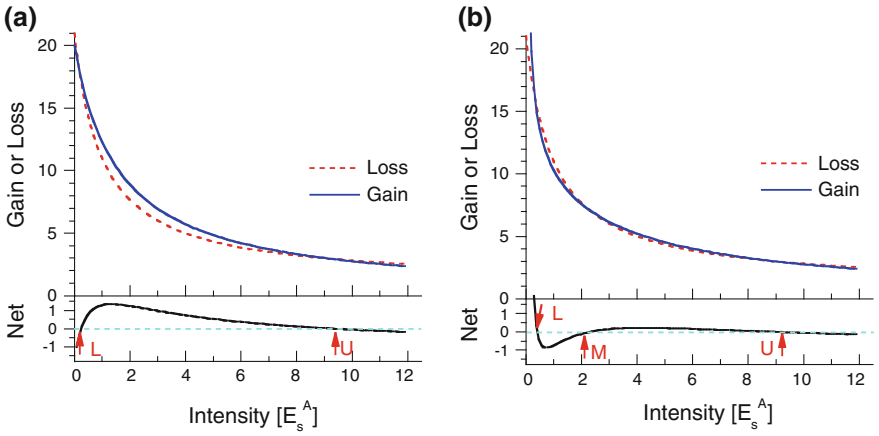

Fig. 2.8 Saturation of the absorption and **a** single-component gain and **b** two-component gain. The intensity is in units of the absorber's saturation intensity and the gain and loss are in units of the nonsaturable loss. The *lower* panels in **a** and **b** show the net gain (gain minus loss). The points where the net gain is zero are stable and labeled

respectively, as described in "Gain and Absorption Dynamics". Both time constants are fast compared to the measured width of the dark pulse, thus the approximation of fast dynamics is still valid; however, the model can better account for this behavior if the gain saturation includes two components with differing saturation powers. Furthermore, the gain will show very slow saturation determined by the carrier injection rate, which means a slow gain saturation part should be included in the gain simulation model. We model this effect by including a term that saturates based on the total energy in the cavity, rather than the instantaneous power. A split-step algorithm simulates each round trip through the laser cavity, calculating the saturation terms in the time domain and the spectral filtering in the frequency domain. Given an arbitrary input condition, usually a pulse, we track the evolution through many round trips until the change between successive round-trips is negligible. To test that the simulation is working properly, we verified that it did produce stable bright pulses with pulse parameters in agreement with previously published results [19].

We find that the simulation produces stable dark pulses when we include the two-component fast gain saturation and the slow saturation. Examining how the gain and absorption saturate, as is often done when discussing the stability of bright pulses in a mode-locked laser, gives insight into why the two-component saturation results in stable dark pulses. In Fig. 2.8, we plot the gain and absorption as a function of intensity for (a) single-component gain saturation and (b) two-component gain saturation. The net gain is plotted in the lower panel for each case. In both cases, the absorption is given by the first two terms in Eq. 2.1 and the intensity is normalized to E_a. Figure 2.2a shows the saturation curves for the situation where the absorber has lower saturation intensity than the gain, but the unsaturated absorption is higher than the unsaturated gain. For this situation, there are two intensities at which the gain and loss cross. Below the lower point,

denoted by "*L*" in Fig. 2.2a, the net gain is negative, so intensities in this range will decay to zero. Above intensity *L*, but below the upper crossing point, denoted by "*U*", there is net gain, so intensities in this range will grow until they reach intensity *U*. Above *U*, the net gain is again negative, so intensities will decay back to point *U*. It is easy to see that an initial bright pulse, or fluctuation, that exceeds intensity *L* will grow until its peak intensity reaches intensity *U*. This simple picture yields a threshold behavior, which produces a rectangular bright pulse. The spectral filter limits the rise and fall times of the pulse, resulting in a smooth pulse with a minimum duration determined by the bandwidth of the spectral filter.

By similar reasoning it initially appears that these conditions would also support a dark pulse. Consider CW operation at intensity *U*, which is stable, with a fluctuation that drops below point *L*. Again the threshold will drive the fluctuation to zero intensity, resulting in a rectangular dark pulse when the spectral filter is omitted. However, in contrast to the bright pulse, simulations show that the inclusion of the spectral filter actually destabilizes the dark pulse, causing it to evolve into a bright pulse.

Stable dark pulses appear in the simulation when we include two-component fast saturation and slow saturation in the model. Figure 2.2b shows the saturation curves for conditions that give a stable dark pulse. A third crossing point, denoted by "*M*" in Fig. 2.8b, occurs with net loss below it and net gain above. CW lasing at intensity above *M* will evolve to intensity *U*. If an intensity fluctuation occurs that crosses below *M*, it will evolve toward *L*. Again, if the spectral filter is omitted, a rectangular dark (gray) pulse will result. However, the inclusion of the spectral filter results in a stable, smooth dark pulse. The evolution of an initial bright pulse into a stable dark (actually gray) pulse is shown in Fig. 2.9a.

We have systematically explored parameter space to determine whether the formation of dark pulses is a robust phenomenon. For each parameter set, we run the simulation until a steady state evolves. We then categorize the steady state as being (1) CW, defined as having an intensity modulation less than 10%, (2) a dark pulse, defined as a dip in the intensity of greater than 10% with dark duration that is less than 40% of the round trip time, (3) a bright pulse, defined as a positive going excursion in the intensity of greater than 10% with bright duration that is less than 40% of the round-trip time, or (4) a pulsation, which is a modulation of greater than 10% that does not fulfill the criteria for a bright or dark pulse. Note that our definition of a dark pulse allows for a gray pulse and the definition of a bright pulse allows it to ride on a CW background. In Fig. 2.9b and c, we plot a "phase space" diagram for the laser showing what output it gives as we vary the two fast gain saturation parameters (larger fast gain saturation intensity I_{gh} and smaller fast gain saturation intensity I_{gl}, both are normalized to the absorption saturation parameter I_q). As I_{gh} increases, the laser goes from CW, to dark pulses, to pulsations and finally to bright pulses. This sequence remains the same as I_{gl} is varied, although the transition between the regimes occurs at a higher I_{gh} as the I_{gl} is increased. We have also varied other parameters and find that the basic structure of this map does not change. The contours in the dark pulse region are lines of constant modulation depth. The darker shaded regions have a modulation closer to one (black pulse). The dark pulse modulation depth is increased (the dark pulses change from gray pulses to black pulses) when I_{gh} and I_{gl} are increased.

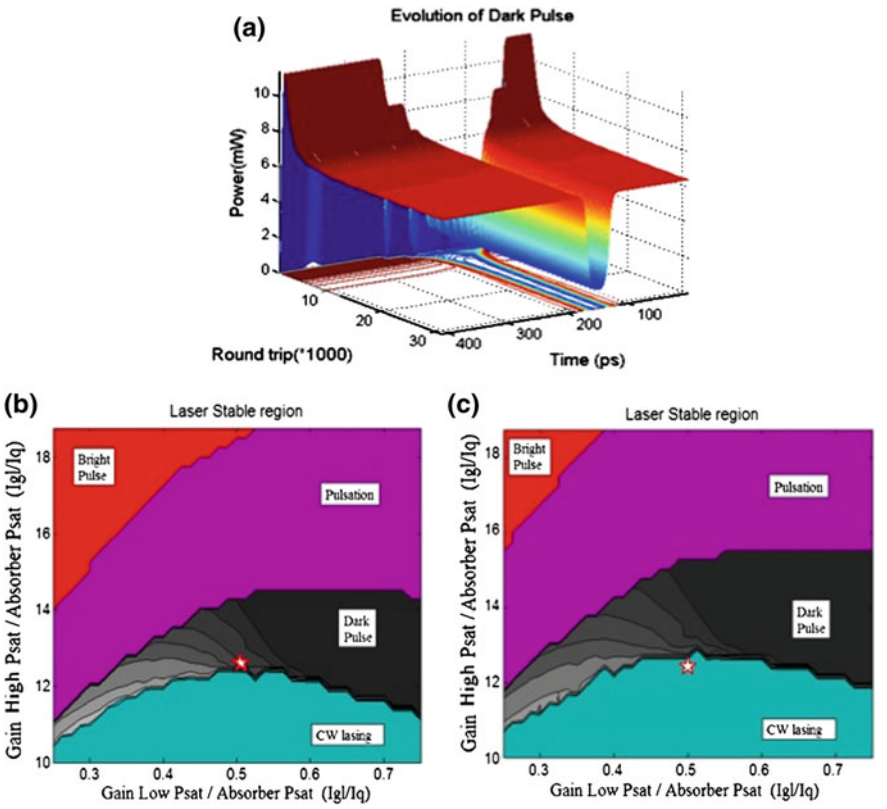

Fig. 2.9 Simulation results. **a** Evolution of initial bright pulse seed into a steady-state solution showing a gray pulse. **b** Phase space map showing stable solution for various parameters. Star indicates the best estimate of the operating point for the experimental conditions when the laser produces dark pulses. **c** Phase space map and estimated operating point for increased injection current, where laser produces a CW output

We have made our best estimate of the operating parameters corresponding to the experimental observation of dark pulses (see supplementary material) and mark it with a star in Fig. 2.3b. It falls well within the region predicted to produce dark pulses. Experimentally, it is difficult to systematically vary the operating parameters. We did increase the injection current and find that a transition from dark pulses to CW operation occurs. A higher injection current means a higher slow gain. In Fig. 2.3c we show the phase space diagram for a higher slow gain where CW operation occurs and find that our best estimate of the operating point falls within the region predicted for CW operation.

Our results experimentally demonstrate a new operating regime for lasers, namely the generation of a train of dark pulses. The theoretical analysis shows that dark pulses are solutions to the master equation describing mode-locked lasers and simulations show that dark pulses are stable. It is the complex dynamics of the QD active region that stabilizes the dark pulse train.

Bistable Quantum Dot Lasers

Introduction

Wavelength bistable lasers are attractive devices for incorporation in next generation optical networks where the time-consuming and component-intensive tasks of optical-to-electrical and electrical-to-optical conversion need to be minimized [20]. They may be employed as compact and fast wavelength switching devices or as memory elements in photonic circuits, due to their robust latching properties [21, 22]. For such devices to be cost competitive they should also be compatible with chip-level optical architecture. Therefore, monolithic devices such as semiconductor diode lasers are more desirable than other types of optical bistable lasers, such as fiber lasers and external cavity lasers [23]. Conventional diode lasers do not normally exhibit wavelength bistability, so we must look to a design with added flexibility while still being monolithic. Two-section diode lasers that are currently being used to generate ultrafast mode-locked pulses are a potential candidate. Working with mode-locked lasers also offers the additional advantage of being able to support extremely high-speed applications.

In two-section diode lasers, the ability to separately control the gain and absorbing regions can lead to various forms of optical bistability. In particular, these lasers can exhibit power bistability when the current applied to the gain section is swept [24, 25]. Wavelength bistability has been more difficult to achieve, but was observed in continuous-wave, two-section distributed feedback (DFB) diode lasers almost two decades ago [26]. There have been relatively few results on bistable wavelength diode lasers since then. In the last few years, the success of mode-locked, two-section QD diode lasers has led to new and exciting results in the area of wavelength bistability [27]. For example, bistability was recently demonstrated between the ground and ES transitions of the QD gain medium [28]. In this case the subordinate mode was not completely quenched throughout the bistable region, possibly due to the fact that cross-gain saturation between ground and ESs was not strong enough. In our earlier work, we reported wavelength bistability from a two-section QD diode laser with a very high contrast between two lasing wavelengths both supported by the ground state (GS) gain [29].

In this section, we present a full investigation of wavelength bistability in two-section QD diode lasers. We first analyze simplified coupled mode equations as a model for the observed bistability. With this simple understanding we can explain why the unique gain dynamics of QD ensembles lead to some of the new results. We then present our experimental results on wavelength bistability from three different two-section passively, mode-locked diode lasers. The devices are not always mode-locked, but when we study the bistability, we only investigate devices working in the stable mode-locked region. All three lasers show wavelength bistability when the reverse bias voltage on the saturable absorber is swept, but they have different wavelength spacings between two bistable branches. Because our lasers operate in the mode-locked region, there are a group of longitudinal modes in one lasing wavelength. Here, the word “mode” refers to one lasing wavelength.

Mode Competition

To gain a general understanding of the important features of our bistable laser, we analyze a simplified set of coupled differential equations [30]. The two-section laser contains regions of both saturable gain and absorption in which lasing modes experience gain or loss and interact with each other. If we include both gain and absorption regions in the same term, assume fast dynamics in the gain and saturable absorber, and make a "weak" saturation approximation, then the intensities of two lasing modes, I_1 and I_2, evolve according to rate equations

$$\frac{dI_1}{dt} = (\alpha_1 - \beta_1 I_1 - \theta_{12} I_2) \times I_1, \tag{2.3a}$$

$$\frac{dI_2}{dt} = (\alpha_2 - \beta_2 I_2 - \theta_{21} I_1) \times I_2, \tag{2.3b}$$

where α_i is the small-signal gain minus loss for each mode, and β_i and θ_{ij} represent the self- and cross-saturation coefficients. These are the Lotka-Volterra equations, which are often used to describe competition between biological species [31]. For certain values of the constants in Eq. 2.3a, there are exactly two steady-state solutions that are characterized by nonzero intensity in only one of the two potential modes. These solutions correspond to one mode (species) always winning out over the other regardless of initial conditions. We are interested in the case in which both modes are simultaneously stable. If this solution is stable to small perturbations, then both modes will coexist in the steady state. If this point is not stable, the system will progress toward one or the other solutions with its ultimate destination being determined by initial conditions. Bistability occurs in this regime.

To reveal the conditions required for bistable operation we can perform a perturbation analysis around the dual mode solution. This point is unstable, and therefore bistable behavior is predicted if

$$\frac{\theta_{12}\theta_{21}}{\beta_1\beta_2} > 1. \tag{2.4}$$

This condition requires the cross-saturation between the two modes to be stronger than the self-saturation. Obviously achieving this condition is quite difficult in a single-section laser. On the other hand, if we include a separate saturable absorption region, the cross-saturation term now consists of two terms

$$\theta_{12} \approx \theta_{21} = \theta_{12}^{g} - \theta_{12}^{a}, \tag{2.5}$$

as does the self-saturation term

$$\beta_1 \approx \beta_2 = \beta_1^{g} - \beta_1^{a}. \tag{2.6}$$

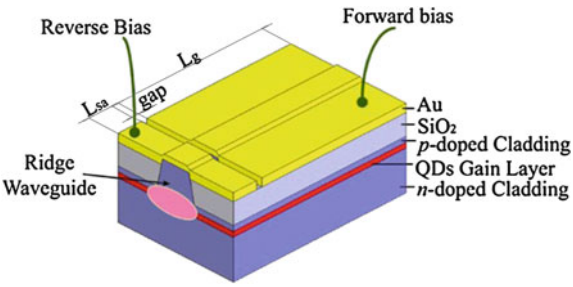

Fig. 2.10 Schematic of the two-section quantum dot diode laser

These add flexibility such that Eq. 2.6 can be satisfied in a system with strong cross-saturation in the gain region and weak cross-saturation in the absorption region. One final consideration is that the overall gain in the two potential modes must be similar. Without this balance, the dual-mode solution will no longer satisfy Eq. 2.4, and stable single-mode operation will prevail.

It is possible to extend the analysis presented here by including full saturation of the absorption and gain [32]. This model predicts more exotic forms of bistability such as that observed in Ref. [28] where single-mode and dual-mode operation are bistable with respect to each other.

Device Structure and Characterization

We fabricated and tested three different two-section QD lasers. A schematic of a generic laser design is shown in Fig. 2.1, as in [29]. It consists of a two-section ridge waveguide where one section is electrically pumped while the other section is reverse biased as a saturable absorber. The active region of all devices consists of a 10-fold stack of InGaAs QD layers embedded in a GaAs waveguide, which is sandwiched between $Al_{0.7}Ga_{0.3}As$ cladding layers. The epitaxial structure is identical to the one used in the extended cavity configuration in order to generate dark pulses. The waveguide was fabricated by standard photolithography and wet etching. A strip waveguide was etched in the top cladding layer followed by the removal of a small section of the heavily doped cap layer to provide isolation between the two sections. The lengths of the gain section and the saturable absorber section are L_g and L_{sa}, respectively. *P*-and *n*-type ohmic contacts were established with Ti/Au and Ni/AuGe/Ni/Au, respectively. No coating was applied to the cleaved facets. The device was mounted *p*-side up on a copper heat sink that was thermoelectrically temperature controlled (Fig. 2.10).

The same QD material was used in all three devices. The QDs have a GS transition at $\sim$ 1,170 nm, with a full-width at half maximum of 60 nm, as determined by a fit to the low excitation electroluminescence data in Fig. 2.2. At higher injection levels, an ES centered at approximately 1,050 nm becomes apparent. This broad, inhomogeneous, gain spectrum is indicative of the size/shape distribution of the QD ensemble.

Table 2.1 Relevant parameters for the three devices tested in this section

	L_g(mm)	L_{sa}(mm)	Guide width (micrometers)	J_{th}(A/cm^2)
Device 1	5.5	0.3	6	136
Device 2	5.5	0.3	6	142
Device 3	2.8	0.3	8	290

It is interesting that the gain spectrum becomes fairly flat over an approximately 200 nm range at injection levels around 300 A/cm^2. This situation leads to interesting mode competition effects in the laser cavity as discussed above. Wavelength bistability is studied in three different laser geometries. The relevant parameters for the three different lasers are summarized in Table 2.1. All three lasers exhibit similar characteristics, thus we will discuss the general features of the first device in-depth as a representative example and then compare and contrast all three devices.

Device 1

The first device we tested has a waveguide width of 6 μm. The length of the gain section (L_g) is 5.5 mm, and the length of the saturable absorber section (L_{sa}) is 0.3 mm. The operating temperature is 12°C. With the saturable absorber region electrically floating, the threshold current is 45 mA (threshold current density is 136 A/cm^2), and the lasing wavelength is 1,173 nm.

The optical spectrum and output power of the QD laser were measured with current injection into the gain section and a reverse-bias voltage applied to the saturable absorber section. With a fixed reverse bias on the saturable absorber.

The optical spectrum and output power of the QD laser were measured with current injection into the gain section and a reverse-bias voltage applied to the saturable absorber section. With a fixed reverse bias on the saturable absorber, the laser exhibits a hysteresis loop in the power-current characteristics [33, 34]. This typical behavior for mode-locked diode lasers can be attributed to the strong hole-burning in the absorber region that allows the laser to stay above threshold even when the injection level is brought below the unsaturated zero-gain point.

When the laser is operated with fixed injection current to the gain region and a varying bias on the saturable absorber region, hysteresis and bistability are observed in the lasing wavelength, as shown in Fig. 2.3a. Throughout the saturable absorber bias range of −6 to −1 V, the laser has two stable wavelengths, 1,163 and 1,173 nm.

By comparing with the electroluminescence data in Fig. 2.2, it is clear that ground-state emission is responsible for both lasing states. As is evident from Fig. 2.11b, the two lasing modes are well separated, and the power contrast between them is more than 30 dB. The switchable wavelength range remains relatively constant throughout the region and is around 7.7 nm when $V_{sa} = -3$ V.

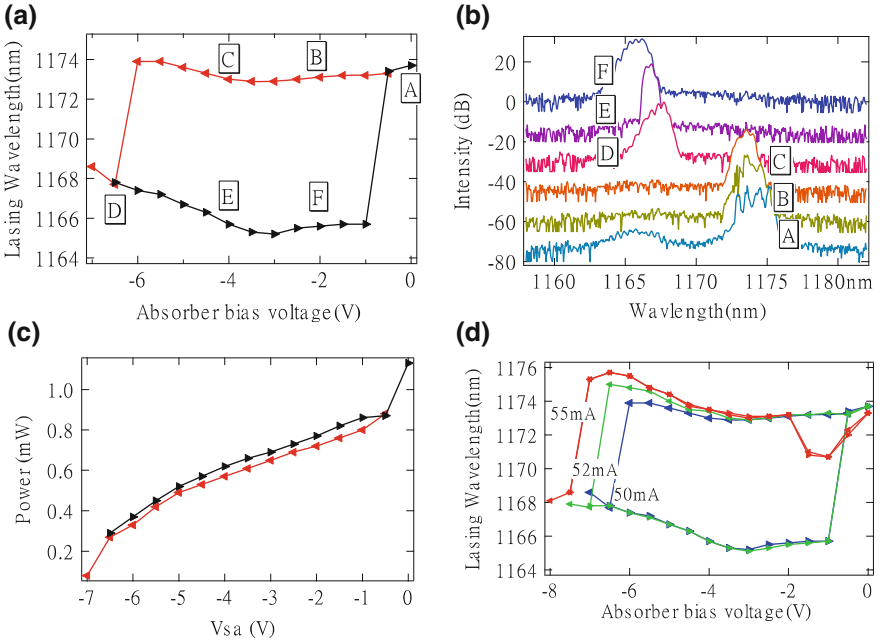

Fig. 2.11 **a** Wavelength of laser emission as a function of saturable absorber bias (V_{sa}) at a fixed gain section current of 50 mA. **b** Optical spectra at various positions in the *left* hysteresis curve (the curves are offset for clarity). **c** Optical power as a function of V_{sa}. **d** Lasing wavelength vs V_{sa} at different gain currents. The *left-pointing triangle* means the trace is taken with the bias ramped up, from 0 to −7 V; The *right-pointing triangle* means the trace is taken with the bias ramped down, from −7 to 0 V

Moreover, the power in each of the two lasing modes is almost identical, as shown in Fig. 2.11c. For example, at $V_{sa} = -4$ V, the power ratio between 1,173 nm (0.57 mW) and 1,166 nm (0.62 mW) is 0.92.

We also found that wavelength bistability can be observed only in the narrow range of gain currents between 50 and 52 mA, as shown in Fig. 2.11d. When the current is too low, the laser is either unstable or only one lasing wavelength is observed at a single saturable absorber bias voltage. When the current is too high, e.g., at the 55 mA shown in Fig. 2.11d, the lasing wavelength varies almost continuously as the saturable absorber bias voltage is varied, and there is no bistability. Note that the bistable area at 52 mA is slightly bigger than the area at 50 mA, with the higher energy mode surviving at larger reverse biases. This is easily explained by the additional gain provided to the shorter wavelength mode at higher injection levels due to the strong state-filling effects in QDs. Therefore, the points where the gain of the two modes becomes dissimilar to support bistable operation moves to lower reverse bias voltage.

We also measured the pulse characteristics of the laser output in the two branches of the hysteresis loop shown in Fig. 2.11. We observed that stable

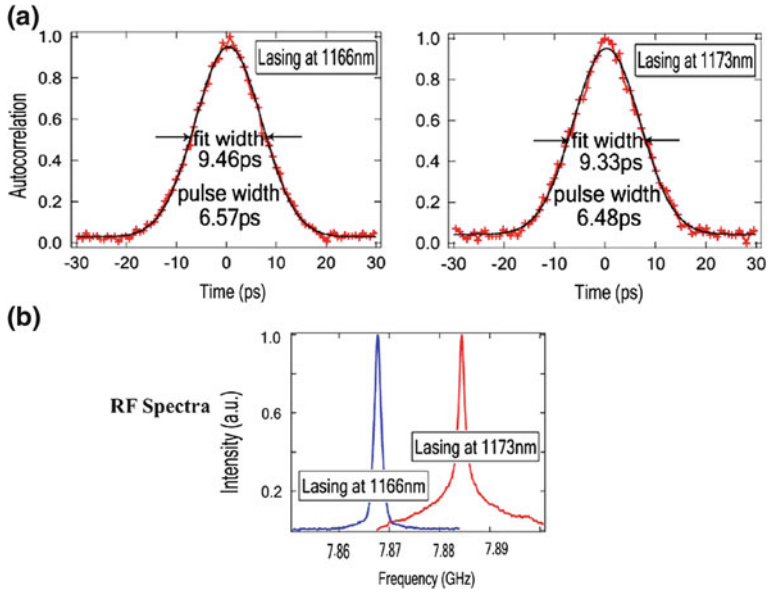

Fig. 2.12 **a** Intensity autocorrelation for the mode-locked pulses on different branches of the hysteresis curve, both at −4 V *reverse* bias. **b** Corresponding radio-frequency spectra

mode-locking occurs in both branches of the hysteresis loop. An autocorrelation trace measured with the laser operating in each branch at $V_{sa} = -4$ V is displayed in Fig. 2.12a. The corresponding pulse width is about 6.5 ps, assuming a Gaussian pulse shape, and is essentially identical in both branches. The pulse could be shortened by increasing the reverse bias, and the shortest value obtained is 3 ps at −6 V. Figure 2.12b shows the radio-frequency (RF) spectra of the device. It indicates a pulse train with a repetition rate of around 7.9 GHz corresponding to a round-trip time of 120 ps. The difference in frequency between the two branches is approximately 15 MHz, with the longer wavelength branch at higher frequency, as expected from the normal dispersion in the GaAs waveguide.

Devices 2 and 3

We tested two other lasers exhibiting bistability (see Table 2.1), a laser that was nominally identical to the first one but with a higher threshold current (device 2) and one with a different ratio of gain length to absorber length (device 3). As expected, device 2 showed qualitatively similar performance to device 1. Bistability is observed at current injection levels between 55 and 64 mA, which is a slightly higher injection level than for device 1. Figure 2.13a compares the two hysteresis curves. Device 2 exhibits a much larger wavelength spacing between the modes, with the shorter wavelength mode at approximately the same location. This

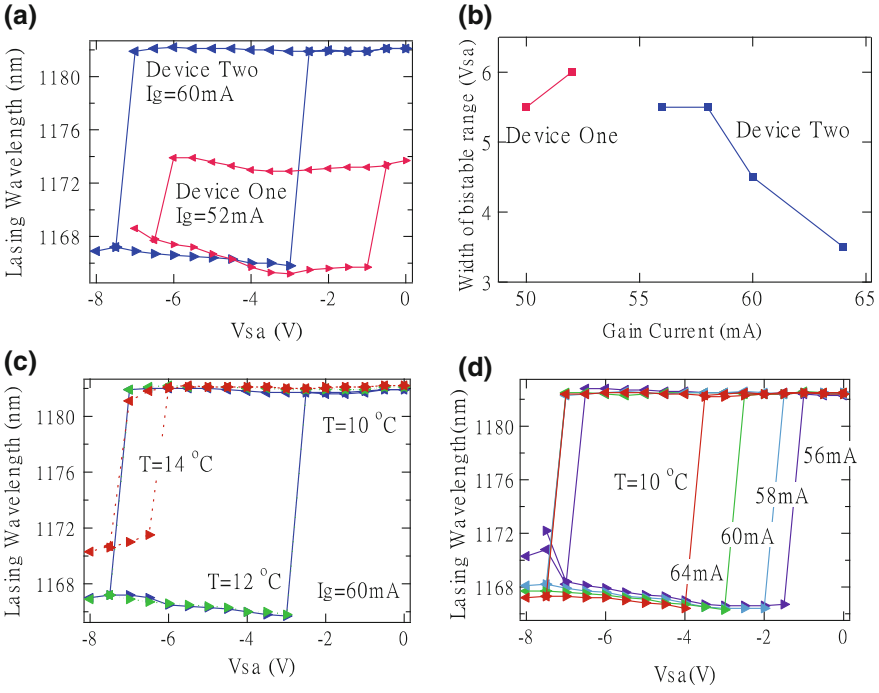

Fig. 2.13 Wavelength bistability comparison between device 1 (in *red* line) and device 2 (in *blue* line). **a** Laser emission as a function of saturable absorber bias (V_{sa}). **b** Width of bistability at different gain current injection. Device 2's lasing wavelengths as a function of saturable absorber bias (V_{sa}). Wavelength bistability data for device 2: **c** At different temperatures (gain current 60 mA). **d** At different gain currents. The *left-pointing triangle* means the trace is taken with the bias ramped up from 0 to −8 V. The *right-pointing triangle* means the trace is taken with the bias ramped down from −8 to 0 V

result is consistent with the higher injection level producing a wider gain bandwidth due to stronger state-filling effects at higher current. These results clearly demonstrate the ability to tune the switchable range in this laser by simple adjustments to the amount of gain and/or loss present in the device.

In Fig. 2.13b, we compare the width of the bistability region for the first two devices as a function of current injected to the gain section. The bistable region decreases with injection current for device 2, which is the complete opposite behavior of the first device. The reason for this difference is that the hysteresis loop for device 2 collapses on the low energy side while device 1 shuts down on the higher energy side. Again, this is consistent with the higher energy mode beginning to dominate at higher injection levels. The detailed bistable data for device 2 are present in Fig. 2.13c for different device temperatures and Fig. 2.13d for different gain currents.

The third laser we tested had a different geometry, with $L_{sa} = 0.3$ mm, $L_g = 2.8$ mm, and a waveguide width = 8 μm. With the saturable absorber region floating and a temperature of 10°C, the threshold current is 65 mA (threshold

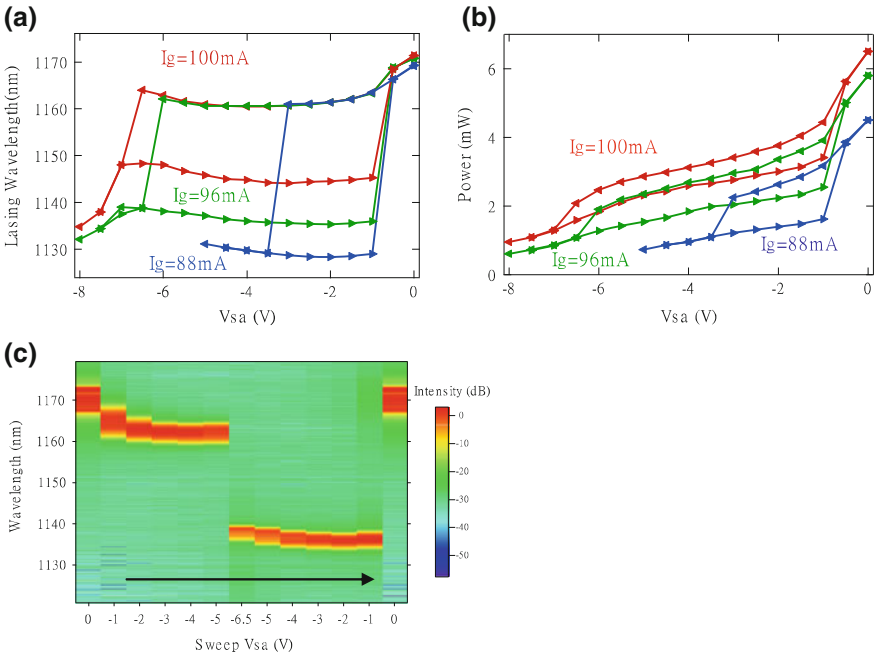

Fig. 2.14 Device 3 lasing wavelengths as a function of saturable absorber bias (V_{sa}). **a** Different gain currents when the temperature is 10°C. **b** Power bistability at different currents. **c** 3D optical spectrum when V_{sa} is swept from 0 to −6.5 V and back to 0 V at $I_g = 96$ mA. The direction is shown by the arrow (the intensity is on a log scale). In **a** and **b**, the *left-pointing triangle* means the trace is taken with the bias ramped up from 0 to −8 V; The *right-pointing triangle* means the trace is taken with the bias ramped down from −8 to 0 V

current density is 290 A/cm^2). This threshold current density is about twice that of the first device because more injection current is needed to overcome the mirror loss due to a shorter gain segment. The initial lasing mode is at 1,170 nm, which is slightly shorter than those of the first two devices. The reason is that the gain region current density is much higher for the third device, and the overall gain peak blue shifts because of state filling. With the significantly higher current density injection, the overall gain profile is much larger and flatter compared to the first two devices (see the EL spectra in Fig. 2.2), resulting in a very large wavelength range in which modes experience similar amounts of gain. This fact leads to more complicated and interesting properties for device 3.

The wavelength-bias voltage hysteresis curve for the third device taken at various injection currents is shown in Fig. 2.14a. The switchable range is 32 nm when the gain current is 88 mA (current density is 393 A/cm^2). When the current is increased to 96 mA (current density is 428 A/cm^2) and 100 mA (current density is 446 A/cm^2), the ranges change to 25 and 16 nm, respectively. The gain region current range for wavelength bistability is from approximately 84–104 mA. Throughout this region, the spacing between laser modes takes on three discrete values, as shown in Fig. 2.14a.

We also show the power-bias voltage hysteresis curve in Fig. 2.14b for different pump currents. The power difference between the two branches is the largest at low current. The difference decreases monotonically as the current is increased while the wavelength difference in the two branches decreases. To demonstrate the high isolation between the two lasing branches, a 3D optical spectrum is plotted for $I_g = 96$ mA in Fig. 2.14c. The black arrow shows the direction of the sweep for the saturable absorber bias. The modes in the two branches are well distinguished and isolated.

The most interesting property of this device is that the switchable range changes with gain current, which did not happen with the first two devices. As the injection to the gain region is increased, the separation between the lasing modes becomes smaller. The longer wavelength mode stays relatively constant, while the shorter wavelength mode moves progressively longer. This behavior is different than the trend observed in the first two devices. It is also counterintuitive, since one would expect higher energy modes to have relatively more gain at higher current densities, due to state filling.

There are two factors that, in combination, may be responsible for these results. At these higher current densities the gain curve is fairly flat, and therefore subtle changes can dictate which mode becomes the eventual winner. Because the gain curve is flat, the relative amounts of gain and loss determine where the gain peak occurs. Since the loss in the absorber region is monotonically increasing in this region (unlike the gain), the net gain peak shifts to lower energies as the relative strength of the absorption grows. This scenario fits well with the observation of higher energy modes lasing as the gain is increased (absorption relatively decreased).

Switching Mechanism

An additional requirement for a practical bistable laser is an effective switching mechanism. The lasers in this work can be switched electrically by modulating the bias voltage on the absorber. There is a strong red shift of the QD transition energy with the application of an electric field. This shift is known as the quantum-confined Stark effect (QCSE) and has been measured to be up to 2 nm/V in similar structures [35]. The effect on the overall laser cavity (i.e., saturable absorber plus gain region) is to shift the peak gain to shorter wavelengths. Once one laser mode becomes too highly favored over the other, bistability breaks down and single mode operation occurs, causing the laser to abruptly change modes.

To measure this shift, we monitored the electroluminescence spectrum as a function of saturable absorber bias from the first laser. In this experiment, one of the facets was antireflection coated to inhibit lasing, and light was extracted from the facet adjacent to the saturable absorber region. The result is shown in Fig. 2.15. Although not a quantitative measure of the gain spectrum in our laser cavity, it is clear that the effect of the increased bias is not only to reduce the overall gain, but also to shift the peak. This peak shift explains why the low-bias lasing mode is always red-shifted compared to the high-bias lasing mode.

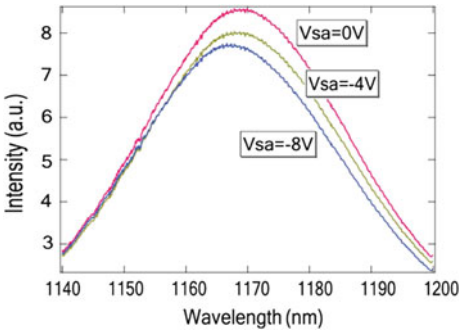

Fig. 2.15 Electroluminescence spectra taken from a sample similar to the first laser, but with an antireflection coating to inhibit lasing. The light was extracted from the facet adjacent to the saturable absorber region. V_{sa} is the bias voltage of the saturable absorber region

Switchable Spacing

The three devices were made from the same wafer, but because of their different structures, the characteristics, including threshold current density and lasing wavelength, of the three lasers were different. Nevertheless, at different pump-current densities, all three devices showed lasing-wavelength bistability. There is also a remarkable characteristic that stands out when the switchable spacings of all three devices (Fig. 2.16) are plotted together. First, the spacing between modes for devices 2 and 3 at the lowest current overlap almost exactly throughout the entire bistable range. Second, the switching occurs in discrete steps. Observed values are 7, 16, 25, and 33 nm; all are roughly multiples of 8–9 nm. This behavior is especially interesting, because there are only two modes lasing at one time. The spacing is maintained for widely spaced modes even without the intermediate modes being active.

Time-resolved and spectral hole-burning measurements have shown that the homogeneous linewidth of InGaAs self-assembled QDs is roughly 10 nm at room temperature [36]. The reverse biased section is depleted of carriers; therefore, this width is a reasonable value to assume for the QDs in this section of the laser. To avoid excessive cross-saturation in the absorber region, modes must be spaced by more than the homogeneous linewidth, a criterion for bistable operation, as explained above. With this reasoning we could expect to never observe bistability of two modes that are separated by less than about 10 nm. This fact would also explain the similar spacing seen for different devices, as it is the optical properties of the QDs that set the scaling.

More difficult to explain is the consistent spacing of widely separated modes in integer multiples of 8–9 nm. This strongly suggests that although only two modes are seen to lase at one time, the other dormant modes still play a role in the laser dynamics.

Switching Time

The wavelength hysteresis loop for a QD diode laser could be used for applications that require switching between wavelengths on a short timescale. When the saturable absorber is biased in the middle of the hysteresis loop, the output

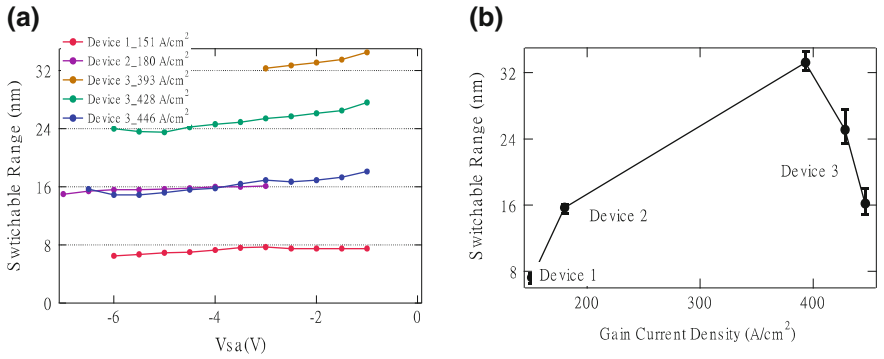

Fig. 2.16 Comparison of the switchable range of the three devices. **a** Different saturable absorber bias voltage. **b** Different gain-current densities. The error bars are the maximum and minimum ranges

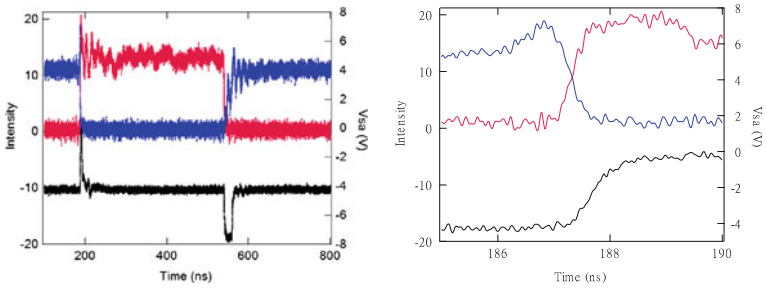

Fig. 2.17 Switching wavelengths between two bistable wavelengths in device 3. The *red* line is the intensity of *long* wavelength branch (1,170 nm), the *blue* line is the intensity of *short* wavelength branch (1,140 nm), and the *black* line is the V_{sa} voltage

wavelength can be switched by an ultrafast electrical pulse of the required polarity. Since no current is injected into the saturable absorber region, the modification of the saturable absorber that selects the lasing mode should be as fast as the pulse injected. Therefore, the lower limit of switching time between the two stable states for a two-section diode laser is determined by the saturation recovery time of the saturable absorber section, as in Ref. [25]. In QDs, carrier recovery time can be sub-picosecond, as measured in "Gain and Absorption Dynamics". In our case, the output of the diode laser is a pulse train, and a minimum of one round-trip is needed for the next lasing state to be established. This timescale is longer than the saturation recovery in our absorber, therefore the wavelength-switching time should be on the order of the round-trip time of the diode laser.

To measure the switching time we dispersed the output of device 3 with a grating and measured each wavelength mode independently. A high-speed electrical pulse was applied to the saturable absorber, and output power data was collected with two high-speed photodiodes and an oscilloscope. The measured switching dynamics are presented in Fig. 2.17. If we define the switching time to

be measured as the time from 90% of the intensity of the wavelength one mode to 90% intensity of the wavelength mode two, then the time to switch from the short wavelength branch to the long wavelength branch is about 150 ps. In this case the switch occurs faster than the voltage pulse, indicating that the jump in wavelength takes place on a narrow voltage range. This measured switching time is only about two round-trips time of the laser.

Conclusion

In conclusion, we have reviewed two novel effects displayed in QD lasers, wavelength bistability, and dark pulse mode-locking. Both these effects are attributable to the complicated recovery dynamics of the QD gain and absorber material. The dark pulse laser was one of the first of its kind and may find application where broadening-free propagation of optical pulses is required in materials with normal dispersion. The bistable laser is electrically switchable within just a few round trips of the cavity and may find use as an optical memory element in next generation optical networks due to its robust latching properties.

References

1. Coldren, L.A., Corzine, S.W.: Diode Lasers and Photonic Integrated Circuits. Wiley, New York (1995)
2. Borri, P., Langbein, W., Hvam, J.M., Heinrichsdorff, E., Mao, M.H., Bimberg, D.: Ultrafast gain dynamics in InAs-InGaAs quantum-dot amplifiers. IEEE Photonics Technol. Lett. **12**(6), 594 (2000)
3. Rafailov, E.U., Cataluna, M.A., Sibbett, W., Il'inskaya, N.D., Zadiranov, Y.M., Zhukov, A.E., Ustinov, V.M., Livshits, D.A., Kovsh, A.R., Ledentsov, N.N.: High-power picosecond and femtosecond pulse generation from a two-section mode-locked quantum-dot laser. Appl. Phys. Lett. **87**(8), 081107 (2005)
4. Schneider, S., Borri, P., Langbein, W., Woggon, U., Sellin, R.L., Ouyang, D., Bimberg, D.: Linewidth enhancement factor in InGaAs quantum-dot amplifiers. IEEE J. Quantum Electron. **40**(10), 1423 (2004)
5. Diels, J.-C., Rudolph, W.: Ultrashort Laser Pulse Phenomena, 2nd edn. Academic, New York (2006)
6. Hall, K.L., Lenz, G., Ippen, E.P., Raybon, G.: Heterodyne pump-probe technique for time-domain studies of optical nonlinearities in waveguides. Opt. Lett. **17**(12), 874 (1999)
7. Kapteyn, C.M.A., Lion, M., Heitz, R., Bimberg, D., Brunkov, P.N., Volovik, B.V., Konnikov, S.G., Kovsh, A.R., Ustinov, V.M.: Hole and electron emission from InAs quantum dots. Appl. Phys. Lett. **76**(12), 1573 (2000)
8. Rafailov, E.U., McRobbie, A.D., Cataluna, M.A., O'Faolain, L., Sibbett, W., Livshits, D.A.: Investigation of transition dynamics in a quantum-dot laser optically pumped by femtosecond pulses. Appl. Phys. Lett. **88**(4), 041101 (2006)
9. Malins, D.B., Gomez-Iglesias, A., White, S.J., Sibbett, W., Miller, A., Rafailov, E.U.: Ultrafast electroabsorption dynamics in an InAs quantum dot saturable absorber at 1.3 mm. Appl. Phys. Lett. **89**(17), 171111 (2006)

10. Borri, P., Langbein, W., Hvam, J.M., Heinrichsdorff, F., Mao, M.H., Bimberg, D.: Spectral hole-burning and carrier-heating dynamics in InGaAs quantum-dot amplifiers. IEEE J. Sel. Top. Quantum Electron. **6**(3), 544 (2000)
11. Haus, H.A.: Mode-locking with a fast saturable absorber. J. Appl. Phys. **46**, 3049 (1975)
12. Kivshar, Y.S., Luther-Davies, B.: Dark optical solitons: physics and applications. Phys. Rep.-Rev. Sect. Phys. Lett. **298**(2–3), 81 (1998)
13. Haelterman, M., Emplit, P.: Optical dark soliton trains generated by passive spectral filtering technique. Electron. Lett. **29**(4), 356 (1993)
14. Weiner, A.M., Heritage, J.P., Hawkins, R.J., Thurston, R.N., Kirschner, E.M., Leaird, D.E., Tomlinson, W.J.: Experimental observation of the fundamental dark soliton in optical fibers. Phys. Rev. Lett. **61**(21), 2445 (1988)
15. Zhang, H., Tang, D.Y., Zhao, L.M., Wu, X.: Dark pulse emission of a fiber laser. Phys. Rev. A **80**(4), 045803 (2009)
16. Ablowitz, M.J., Horikis, T., Nixon, S., Frantzeskakis, D.: Dark solitons in mode-locked lasers. Opt. Lett. **36**(6), 793 (2001)
17. Lenstra, D., et al.: Coherence collapse in single-mode semiconductor lasers due to optical feedback. IEEE J. Quantum Electron. **QE-21**(6), 674–679 (1985)
18. Carroll, O., et al.: Feedback induced instabilities in a quantum dot semiconductor laser. Opt. Express **14**(22), 10831 (2006). 30 Oct
19. Kärtner, F.X., Kopf, D., Keller, U.: J. Opt. Soc. Am. B **12**, 486–496 (1995)
20. Kawaguchi, H.: Bistable laser diodes and their applications: state of the art. IEEE J. Sel. Top. Quantum Electron. **3**(5), 1254 (1997)
21. Kawaguchi, H., Mori, T., Sato, Y., Yamayoshi, Y.: Optical buffer memory using polarization-bistable vertical-cavity surface-emitting lasers. Japan. J. Appl. Phys. Part 2-Lett. Express Lett. **45**(33–36), L894 (2006)
22. White, I., Penty, R., Webster, M., Chai, Y.J., Wonfor, A., Shahkooh, S.: Wavelength switching components for future photonic networks. IEEE Commun. Mag. **40**(9), 74 (2002)
23. Tangdiongga, E., Yang, X.L., Li, Z.G., Liu, Y., Lenstra, D., Khoe, G.D., Dorren, H.J.S.: Optical flip-flop: based on two-coupled mode-locked ring lasers. IEEE Photonics Technol. Lett. **17**(1), 208 (2005)
24. Qasaimeh, O., Zhou, W.D., Phillips, J., Krishna, S., Bhattacharya, P., Dutta, M.: Bistability and self-pulsation in quantum-dot lasers with intracavity quantum-dot saturable absorbers. Appl. Phys. Lett. **74**(12), 1654 (1999)
25. Uenohara, H., Takahashi, R., Kawamura, Y., Iwamura, H.: Static and dynamic response of multiple-quantum-well voltage-controlled bistable laser diodes. IEEE J. Quantum Electron. **32**(5), 873 (1996)
26. Shoji, H., Arakawa, Y., Fujii, Y.: Fast bistable wavelength switching characteristics in 2-electrode distributed feedback laser. IEEE Photonics Technol. Lett. **2**(2), 109 (1990)
27. Huang, X.D., Stintz, A., Li, H., Rice, A., Liu, G.T., Lester, L.F., Cheng, J., Malloy, K.J.: Bistable operation of a two-section 1.3 mm InAs quantum dot laser—absorption saturation and the quantum confined stark effect. IEEE J. Quantum Electron. **37**(3), 414 (2001)
28. Cataluna, M.A., Sibbett, W., Livshits, D.A., Weimert, J., Kovsh, A.R., Rafailov, E.U.: Stable mode locking via ground- or excited-state transitions in a two-section quantum-dot laser. Appl. Phys. Lett. **89**(8), 081124 (2006)
29. Feng, M., Brilliant, N.A., Cundiff, S.T., Mirin, R.P., Silverman, K.L.: Wavelength bistability in two-section mode-locked quantum-dot diode lasers. IEEE Photonics Technol. Lett. **19**(9–12), 804 (2007)
30. Siegman, A.E.: Lasers. University Science Books, Sausalito (1986)
31. Murray, J.D.: Mathematical Biology I: An Introduction. Springer, Berlin (2003)
32. Lin, C.F., Ku, P.C.: Analysis of stability in two-mode laser systems. IEEE J. Quantum Electron. **32**(8), 1377 (1996)
33. Thompson, M.G., Rae, A., Sellin, R.L., Marinelli, C., Penty, R.V., White, I.H., Kovsh, A.R., Mikhrin, S.S., Livshits, D.A., Krestnikov, I.L.: Subpicosecond high-power mode locking using flared waveguide monolithic quantum-dot lasers. Appl. Phys. Lett. **88**(13), 133119 (2006)

34. Thompson, M.G., Rae, A.R., Xia, M., Penty, R., White, I.H.: InGaAs quantum-dot mode-locked laser diodes. IEEE J. Sel. Top. Quantum Electron. **15**(3), 661 (2009)
35. Alen, B., Bickel, F., Karrai, K., Warburton, R.J., Petroff, P.M.: Stark-shift modulation absorption spectroscopy of single quantum dots. Appl. Phys. Lett. **83**(11), 2235 (2003)
36. Borri, P., Langbein, W., Schneider, S., Woggon, U., Sellin, R.L., Ouyang, D., Bimberg, D.: Exciton relaxation and dephasing in quantum-dot amplifiers from room to cryogenic temperature. IEEE J. Sel. Top. Quantum Electron. **8**(5), 984 (2002)

http://www.springer.com/978-1-4614-3569-3

Quantum Dot Devices
Wang, Z.M. (Ed.)
2012, XIII, 370 p. 242 illus., 146 illus. in color.,
Hardcover
ISBN: 978-1-4614-3569-3